MEDICAL ROBOTS

Soft robotic artificial left ventricle simulator capable of reproducing myocardial biomechanics

James Davies[1], Mai Thanh Thai[1], Bibhu Sharma[1], Trung Thien Hoang[1], Chi Cong Nguyen[1], Phuoc Thien Phan[1], Thao Nhu Anne Marie Vuong[1], Adrienne Ji[1], Kefan Zhu[1], Emanuele Nicotra[1], Yi-Chin Toh[2], Michael Stevens[1,3], Christopher Hayward[4,5], Hoang-Phuong Phan[3,6], Nigel Hamilton Lovell[1,3], Thanh Nho Do[1,3]*

The heart's intricate myocardial architecture has been called the Gordian knot of anatomy, an impossible tangle of intricate muscle fibers. This complexity dictates equally complex cardiac motions that are difficult to mimic in physical systems. If these motions could be generated by a robotic system, then cardiac device testing, cardiovascular disease studies, and surgical procedure training could reduce their reliance on animal models, saving time, costs, and lives. This work introduces a bioinspired soft robotic left ventricle simulator capable of reproducing the minutiae of cardiac motion while providing physiological pressures. This device uses thin-filament artificial muscles to mimic the multilayered myocardial architecture. To demonstrate the device's ability to follow the cardiac motions observed in the literature, we used canine myocardial strain data as input signals that were subsequently applied to each artificial myocardial layer. The device's ability to reproduce physiological volume and pressure under healthy and heart failure conditions, as well as effective simulation of a cardiac support device, were experimentally demonstrated in a left-sided mock circulation loop. This work also has the potential to deliver faithful simulated cardiac motion for preclinical device and surgical procedure testing, with the potential to simulate patient-specific myocardial architecture and motion.

INTRODUCTION

Development of cardiac devices, as well as training for surgical techniques, still relies heavily on the use of ex vivo and in vivo animal models (*1*). More recently, there has been a push to develop high-fidelity simulators that replicate the functions of the human heart. Such benchtop simulators have the potential to reduce our reliance on animal models and reduce the ethical, financial, and time costs associated with preclinical trials (*1*). Surgical training also greatly benefits from these kinds of models, improving procedure-specific skills and reducing adverse outcomes (*2*–*4*).

Although several static synthetic heart simulators have been developed in the past (*5*, *6*), such models have very limited usefulness where complex dynamics are desired. Dynamic heart models are a very attractive product for the simulation of different cardiac conditions and diseases, for preclinical cardiac device testing, and for surgical procedure training. Several cardiac simulators created from ex vivo heart models have been developed. However, unless they are artificially paced (*7*), their musculature is passive. Some use compliant membranes that expand and contract inside the chambers of the heart (*8*, *9*), whereas others use pulsatile pumps that either apply pressure to the outer surface of the heart (*10*, *11*) or force blood directly into the heart (*12*, *13*); all of these simulators produce either inverse or nonbiomimetic function. A more detailed comparison of similar existing devices can be found in the Supplementary Materials and table S1. A smaller proportion of these dynamic heart simulators are based on soft robotic mechanisms. Soft robotic actuators have the unique potential to mimic bodily musculature in both form and material properties. Roche *et al.* (*14*) successfully designed a McKibben muscle–based soft robotic analog of the heart's epicardial muscle layer, creating a device capable of ventricular shortening and twisting but no notable radial motion due to the omission of other myocardial layers. This device was then extended to a soft robotic sleeve that was wrapped around the failing heart and included both an epicardial and a transmural McKibben muscle layer (*15*). Although this device was presented as a ventricular assist device and not a simulator, it may be capable of reproducing some, but not all, of the complex motions of the native heart. Critically, this device cannot decouple ventricular twist from ventricular shortening, meaning that it is incapable of achieving true biomimetic function.

Recently, Park *et al.* (*16*) introduced a computational model of a soft robotic left ventricular myocardium. However, this system was unable to integrate a three-layered artificial muscle myocardium (epicardium, transmural, and endocardium) to recapitulate the minutiae of the cardiac cycle. The authors removed one layer of the muscle and reconfigured another, abstracting it from physiology to achieve physiological torsional motion. Further abstraction from physiology can be seen in the device's ventricular lengthening during all phases of systole, which should only occur during isovolumetric contraction (IVC). Conversely, the native heart shortens directly after IVC, contributing to 60% of the ejection fraction (EF) (*17*). In a later work, Park *et al.* (*18*) also developed a soft robotic organosynthetic dynamic cardiac simulator, which could be used as an in vitro testing platform or a surgical training tool. To maintain the internal structure of the real heart, the authors fixed an ex vivo heart with formalin, removed its ventricular musculature, and then integrated a bioinspired soft robotic musculature to provide semibiomimetic motion. Although this fabrication concept is groundbreaking, neither hemodynamic data nor torsional motion data were reported, apart

[1]Graduate School of Biomedical Engineering, Faculty of Engineering, UNSW Sydney, Sydney, NSW 2052, Australia. [2]School of Mechanical, Medical, and Process Engineering, Queensland University of Technology, Brisbane, Queensland 4000, Australia. [3]Tyree Institute of Health Engineering (IHealthE), UNSW Sydney, Sydney, NSW 2052, Australia. [4]Department of Cardiology, St Vincent's Hospital, Sydney, NSW 2010, Australia. [5]St Vincent's Clinical School, Faculty of Medicine, UNSW Sydney, Sydney, NSW 2052, Australia. [6]School of Mechanical and Manufacturing Engineering, Faculty of Engineering, UNSW Sydney, Sydney, NSW 2052, Australia.
*Corresponding author. Email: tn.do@unsw.edu.au

from a physiologically appropriate EF. Furthermore, its soft robotic musculature was designed on the basis of helical ventricular myocardial band (HVMB) theory, which is inconsistent with recent research findings (*19*–*21*), as admitted by the authors. Park *et al.* (*22*) have since constructed a version of this device using McKibben muscles in the same nonphysiological arrangement as their in silico work described previously (*16*). This device was successfully used to simulate mitral valve function and dysfunction as well as surgical intervention and could produce physiological volume and pressure changes. This work is a great example of the utility of benchtop simulators and their potential influence on device development and surgical procedures. However, no data were presented on the longitudinal and torsional motion of the device.

Singh *et al.* (*23*) used the same organosynthetic approach to develop an artificial right ventricular simulator, actuated by McKibben muscles. This work is an important step toward the construction of a biventricular cardiac model. This device could produce physiological pressure and volume changes, as well as pathophysiological conditions, and could be used as a platform for training of valve repair surgery. However, the longitudinal and torsional motion of the native right ventricle (*24*, *25*) was not considered in the placement of the circumferential artificial muscle fibers. In this way, the device does not faithfully capture native right ventricular mechanics.

Furthermore, in recent years, works by Rosalia *et al.* (*26*, *27*) have explored the use of soft robotic simulators that use patient-specific internal cardiac structures that are 3D printed to provide patient-specific hemodynamics and predicted responses to cardiac device implantation. Although this work demonstrates the potential influence of the development of benchtop simulators, the authors' current actuation method is not truly biomimetic and only provides radial volume change, limiting its application to simulations upstream or downstream from the left ventricle (LV).

Currently, no synthetic artificial heart models can faithfully mimic complex three-dimensional (3D) twisting and compressive motions of the native myocardium. Addressing these unmet needs, this paper introduces a soft artificial LV, leveraging the currently accepted continuum model of cardiac musculature (Fig. 1), which is explained in the next section. Instead of using pneumatic artificial muscles (PAMs) such as McKibben muscles, which have previously struggled to reproduce biomimetic motion, we looked to the closest analog of a native myofibril, namely, the hydraulic filament artificial muscle (HFAM), which was previously developed by our team (*28*, *29*). Distinct from the PAMs, this type of soft robotic artificial muscle is scalable with high aspect ratios and high elongation, meaning that we can tune fiber density to provide the appropriate resolution for motion recapitulation. Furthermore, because this muscle operates in depressurization, the material properties can be tuned to provide the desired maximum forces and remove the possibility of causing damage through excessive force generation.

As seen in Fig. 1 (A and B), we used a three-layer simplification of the continuum model of cardiac fiber arrangement as the inspiration for our artificial muscle architecture. We stabilized these three muscle layers using a removable 3D pinboard, with its associated pins directly linking the muscle layers and fixing their fiber angles, similar to the native heart's extracellular matrix (ECM) elastin/collagen networks (*30*, *31*). Both the ventricular shape and its fiber angles can be tuned to simulate patient-specific or disease-specific data. We set these parameters to closely match those of a healthy heart. We then actuated its muscle layers with input that mimics measured canine myocardial strains and evaluated the output motion and function. The results demonstrate this system's ability to faithfully reproduce biomimetic motion and function in a left-sided mock circulation loop (MCL) (Fig. 1D). We also characterized the simulator's ability to reproduce performance consistent with heart failure and simulated the performance of a cardiac support device. Although we have not reproduced all cardiac anatomical features, research by Park *et al.* (*18*) shows that integration of soft robotic musculature with ex vivo structures is possible. Future development in this direction could produce high-fidelity simulators with anatomical structures and the ability to completely replicate motion and function in both healthy and diseased states (Fig. 1D), potentially reducing the reliance on expensive and time-consuming ex vivo or in vivo preclinical testing for cardiac devices and surgical training.

RESULTS

Biomimetic requirements

To mimic the complex motion and function of the native heart in a high-fidelity cardiac simulator, an understanding of the heart's complex structures and motions is necessary. Five centuries of anatomical study have been spent attempting to unravel the Gordian knot of anatomy, as described by Pettigrew (*32*), likening the heart to the legendary knot cut by Alexander the Great, which was so intricately tied that it was impossible to decipher. Although a great deal of attention has been given to the HVMB theory of myocardial architecture in the past (*33*, *34*), many contradictions have emerged in recent research (*19*–*21*). Currently, the most consistent model of myocardial architecture is the continuum model.

Conceived of and popularized by the likes of Pettigrew (*32*), Rushmer *et al.* (*35*), and Streeter (*36*), this muscle fiber continuum across the LV myocardial wall is visualized in Fig. 2A. As evidenced by diffusion tensor magnetic resonance imaging data (*37*, *38*), if we take a section of the LV wall, there will exist a continuum of fiber angles with respect to the heart horizontal axis ranging from $\theta_{epi} = 60^{\circ}$ at the outer layer (epicardium), to $\theta_{trans} = 0^{\circ}$ at the middle layer (transmural), to $\theta_{endo} = -60^{\circ}$ at the inner layer (endocardium). Here, we simplified this continuum structure to a three-layer model, taking the epicardial (Epi), transmural (Trans), and endocardial (Endo) layers of the native LV myocardium.

Looking at Fig. 2B, we can see that, in systole, the Epi helical layer provides ventricular shortening and counterclockwise twisting of the LV. The Trans layer provides ventricular narrowing, which can lengthen the ventricle through a scissoring action between the two oppositely wound Endo and Epi helices. This will be explained further, but it is a key function in early systole. Last, the Endo helical layer provides ventricular shortening and clockwise twisting of the base of the LV. Although this clockwise twisting function is largely overpowered by the Epi layer, it is seen in early systole before the epicardium has contracted. During diastole, in general, these motions are reversed as previously compressed tissues recoil elastically.

Figure 2C describes a more detailed set of LV motions as they occur through the four phases of the cardiac cycle, the first three of which occur during systole, and Fig. 2D shows the ventricular pressure throughout the four phases. The complexity of these motions is dictated by the asynchronous contraction and relaxation of the three simplified layers, stemming from the sequential patterns of electrical conduction through the LV myocardium. More detail can be found in the Supplementary Materials, along with a list of physiological targets for LV motion (table S2).

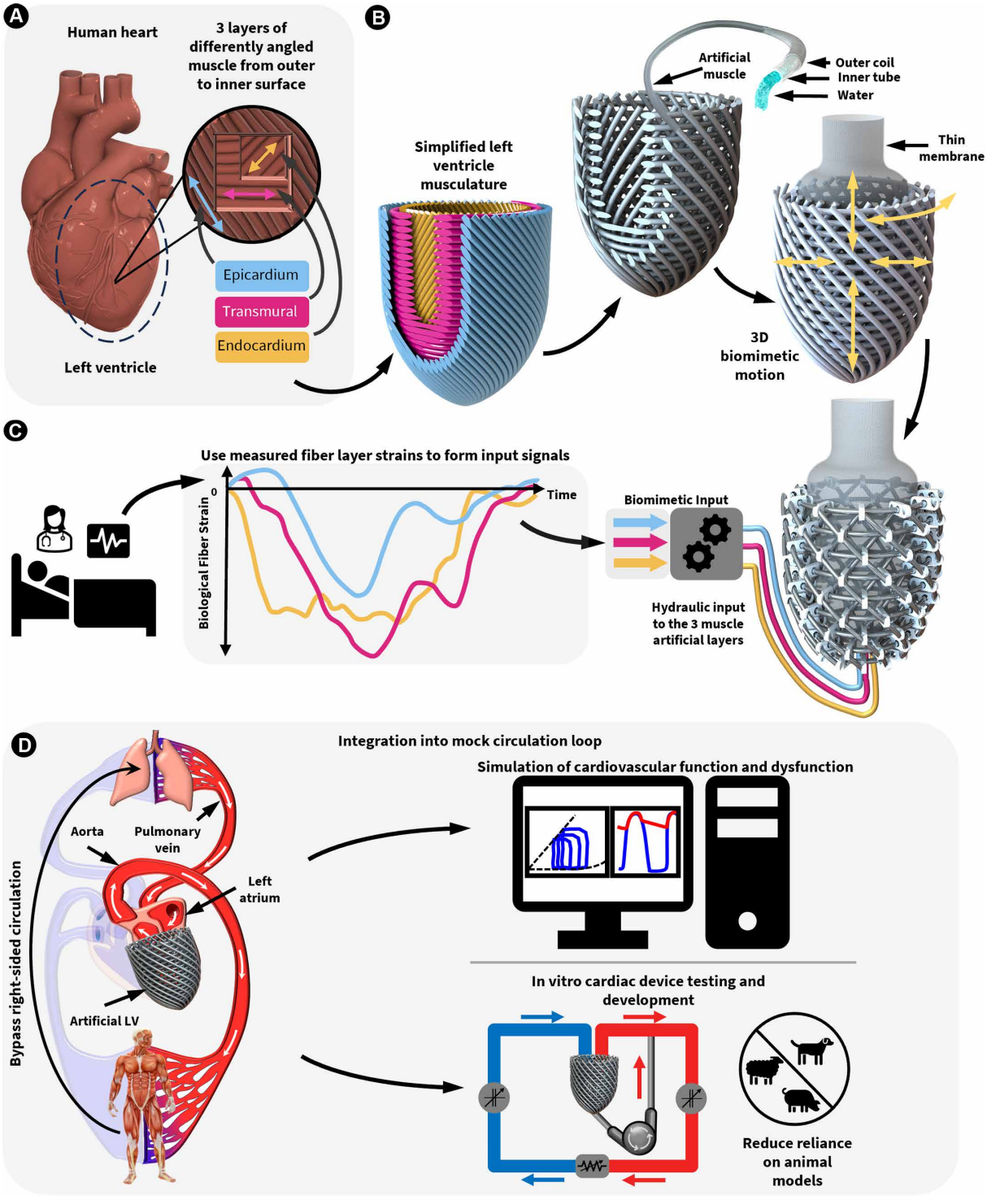

Fig. 1. Overview of device concept and its potential application. (**A**) Simplification of native cardiac musculature into three layers of differently angled muscle fibers (heart model from cadnav.com). (**B**) Inspiration for our artificial LV from a simplified native architecture. (**C**) Biological fiber layer strain data adapted from Ashikaga *et al.* (*39*) are input into each of the three simplified layers of the artificial myocardium. (**D**) Potential use as a test platform for in vitro cardiac device development such as heart pumps, heart valves, or endovascular catheters.

Biomimetic design, fabrication, and control

With these requirements, we have designed and fabricated a new soft robotic device capable of replicating biomimetic motion and function. As shown in Fig. 1 (A and B), we took the simplified three-layer myocardial model and replaced each layer's biological cardiac muscle fibers with HFAMs (*28*, *29*). We selected this actuator because

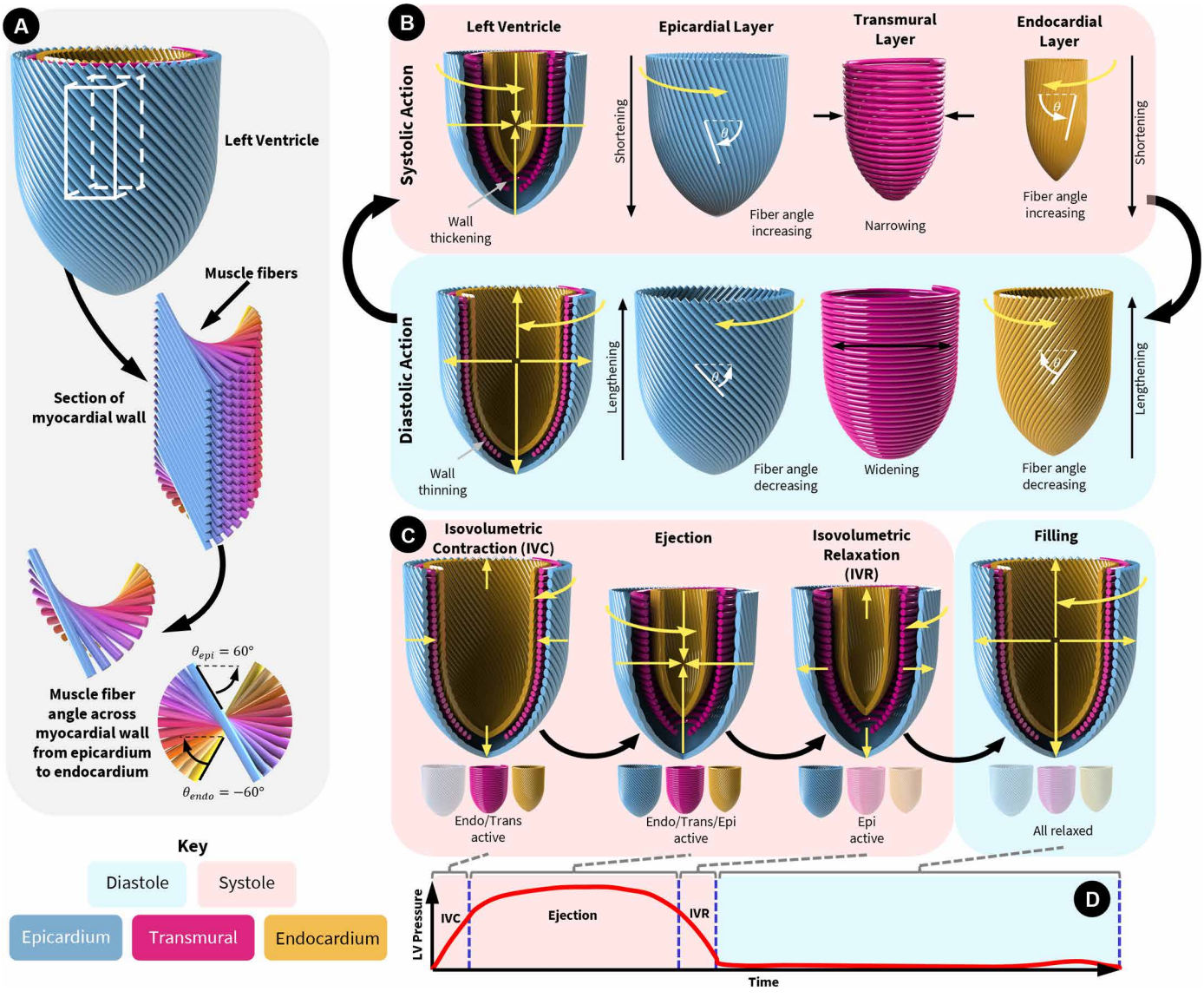

Fig. 2. Overview of native heart form and function. (**A**) Visualization of the muscle fiber arrangement across a section of the native LV myocardial wall from the epicardium to the endocardium. (**B**) Visualization of the general systolic and diastolic functions and contributions of each simplified muscle layer (Epi, Trans, and Endo). (**C**) More detailed visualization of LV motion through the four phases of the cardiac cycle. (**D**) LVP through the four phases of the cardiac cycle.

of its scalability and extremely high aspect ratio capabilities. These muscles can be fabricated at the meter scale, meaning that one single cardiac layer could consist of only one muscle fiber and be controlled by one hydraulic input. The scalability of these muscles also means that the density of fiber lengths in each myocardial layer can be tuned to provide the desired mechanical properties. This type of artificial muscle is inherently safe because it operates in contraction through depressurization (unlike McKibben muscles, which contract upon pressurization), and its force is directly linked to the elastic properties of its components. Thus, we can tune the elastic modulus and spring constant of the inner elastomeric tube and outer helical coil to limit the pumping pressure. Using a hydraulic fluid as the pressurization medium also has advantages over pneumatics, including linearity, sensitivity, and response time.

With this actuation choice, the simplified three-layer LV model can feasibly be replicated in a biomimetic soft robotic system, as shown by the conceptualization in Fig. 1 (A and B). As previously highlighted, if we apply biomimetic input strains to these biomimetic muscle layers, we should see biomimetic output function. Figure 1 (A to C) provides an overview of this biomimetic approach, beginning with the extraction of physiological fiber angles and strains (*39*) for each of the three muscle layers. The measured fiber angles were then programmed into the fabrication process such that our artificial muscle fibers were oriented in the same way. This fabrication process is described in greater depth in Materials and Methods. Then, as seen in Fig. 1C, we drove the muscle layers by pumping in a hydraulic input proportional to the measured physiological fiber strains. Given the linearity of the artificial muscle strain in response to input volume,

this physiologically proportional input causes the LV to move in a physiologically similar manner.

For the purposes of this paper, we set the Epi and Endo fiber angles to those of a typical healthy human heart (± 60°) and set the Trans fiber angle to ~0°. However, these angles and this fiber density can be set to almost any desired angle as determined by patient or disease data.

Range of motion analysis

Our analysis began with the characterization of the range of motions and pressures that the artificial LV musculature could perform. With the apex fixed in place, we used image processing techniques to track the motion of the outer surface of the artificial LV and the twist angle. Figure 3A shows the device as it contracts from its end-diastolic state to its end-systolic state, and Fig. 3B shows the outer surface motion tracking results for the prototype in Fig. 3A in the long- and short-axis plane. This analysis was performed with simultaneous contraction of all three layers from their pressurized end-diastolic state. We observed a 25-mm reduction in diameter of the outer surface at the base of the LV and a 12-mm reduction in its long axis or height.

Figure 3 (D and E) shows this LV volume (LVV) and LV twist, respectively, as they relate to all combinations of input volume to the muscle layers; the Endo, Trans, and Epi muscle layer input volumes form the three spatial axes, and the color axis refers to LVV and LV twist, respectively. The volume and twist results for the simultaneous contraction testing in Fig. 3 (A and B) can be seen in the diagonal line labeled with the three active muscle layers. This simultaneous contraction of all three layers produced the largest stroke volume (SV) of ~100 ml, contracting from an end-diastolic volume (EDV) of 140 ml to an end-systolic volume (ESV) of 40 ml, which equates to an ~70% EF. Figure 3D shows the importance of the Trans layer (the z axis) in generating volume displacement, and the Epi and Endo layers have some, but relatively little, effect. Figure 3E reveals that close to zero LV twist occurs during simultaneous contraction of all three muscle layers but also during pure Trans contraction and in combined Epi/Endo contraction. This demonstrates that the expected torsional mechanics of the device given co-contraction, or no contraction, of the helical Epi/Endo muscle layers should not produce any twist. As expected, whenever the Epi or Endo layers were contracted in isolation, with or without Trans contraction, we saw a large degree of twist. When only the Epi or Endo layers were contracted independently, we achieved 34° and −29° twist, respectively, where counterclockwise twist is positive and clockwise twist is negative. However, when we contracted the Epi or Endo layers in conjunction with the Trans layer, we achieved 49° and −52° twist, respectively. Further data for all combinations of layer contraction can be seen in figs. S1 to S6.

In addition, we characterized the LV's blocked-volume pressure performance for several blocked volumes from the EDV to ESV, as can be seen in Fig. 3F. This testing demonstrates the LV's ability to provide supraphysiological pressures throughout most of its cardiac cycle. This is by no means a characterization of the maximum pressures the LV can produce at each of these blocked volumes. To perform this testing, we lined the inner surface of the LV with a nonstretch plastic bag with a pressure probe and attached a fluid reservoir (valved) to allow for volume adjustments. Starting near the EDV, we inflated all muscle layers to give an internal LVV of 120 ml and then withdrew a set amount of volume from each muscle layer in a simultaneous, sinusoidal manner while measuring the pressure inside the LV. We repeated this for several blocked volumes toward the ESV. Figure 3G reveals the extracted peak pressures generated at each of these volumes. The maximum pressure generated was 317 mmHg, at a 120-ml LVV, greater than 2.5 times typical systolic pressures. We were still able to achieve a peak of 169 mmHg at a 60-ml LVV, which is greater than typical systolic pressures, showing that our device is more than strong enough to simulate physiological pressures. There is also an approximately linear relationship between the peak LV pressure (LVP) and blocked LVV.

We also developed a simplified model of our LV simulator, which is described in detail in the Supplementary Materials and fig. S7 and was used as a predictive design tool. Figure 3C reveals that the simulated LV motion is similar to the physical prototype motion in Fig. 3 (A and D). The model's agreement with experimental data for the range of motion analysis can be seen in figs. S2 and S4 to S6.

Biomimetic motion analysis

Without access to human studies, we adapted the strain data from the layers of a canine heart that correspond to the layers in our device. The work done by Ashikaga *et al.* (*39*) gave us a good starting point in building the input signal. Their study provides myocardial fiber strain data for 10 muscle layer divisions from the endocardium to the epicardium of a canine heart. To adapt these data to a control signal for our muscles, we first identified patterns and features in each of the four stages of the cardiac cycle: IVC, ejection, isovolumetric relaxation (IVR), and filling. With the necessary relationships between the Endo, Trans, and Epi layers identified, we rebuilt the signals using smoothing splines in MATLAB. We performed Fourier analysis on these signals to formulate a continuous, time-domain function of the cardiac cycle with adjustable amplitude, frequency, and phase. Each function was reconstructed using the eight most powerful frequencies. Figure 4F reveals the normalized input volume signals for each of our three muscle layers for one cardiac period. Also seen here is a magnified section of the signals during IVC, with a comparison to Ashikaga's measured data, highlighting the similarities between the two.

From Fig. 4 (A and B), we can see a total LV long-axis shortening of ~14 mm, and the outer surface of the device reduces ~22 mm in diameter in the short axis, from ~82 to ~60 mm. This 14-mm long-axis shortening is close to the atrioventricular plane displacement of 16 mm reported by Carlsson *et al.* (*40*). The short-axis end-diastolic and end-systolic diameters of the inner surface are estimated to be ~56 and ~33 mm, which are close to the respective 50.2 ± 4.1- and 32.4 ± 3.7-mm native heart averages (*41*). These end-diastolic and end-systolic diameters calculated from our image processing were validated against ultrasound imaging of the inner surface (Fig. 4, D and E), with reported diameters of ~57 and 33 mm, respectively.

Figure 4B shows the expected lengthening and narrowing of the ventricle in the IVC phase, as discussed in the Supplementary Materials. The adapted biomimetic input also gave rise to the ~4° clockwise twist of the base of the LV with respect to the apex (Fig. 4H), which can be seen in the physiological data traced from Ingels *et al.* (*42*) and Sengupta *et al.* (*43*) in Fig. 4 (I and J), respectively. After this torsion in IVC, the ventricle then twisted counterclockwise ~17°, which is similar to the peak torsion observed in the study by Sengupta *et al.* (*43*). Then, in IVR, this twist reversed by ~4° before forming a secondary peak, as seen in the region highlighted in blue in Fig. 4H. This pattern is well matched in Sengupta's data (Fig. 4J).

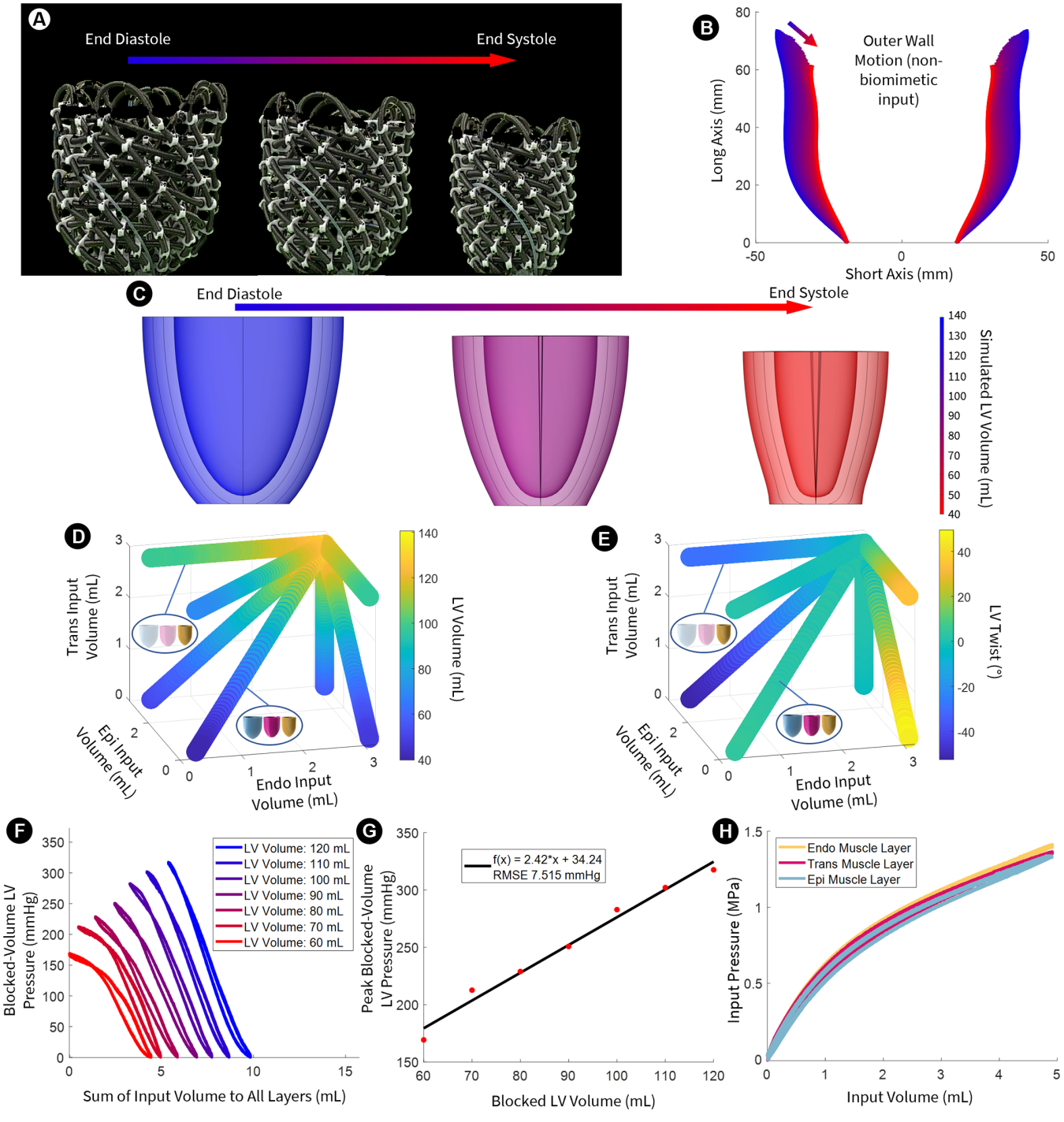

Fig. 3. Range of motion analysis of the artificial LV. (**A**) In vitro motion of the physical prototype from end diastole to end systole. (**B**) Outer surface motion from end diastole (blue) to end systole (red), taken from (A). (**C**) In silico simulated LVV from end diastole to end systole. (**D**) In vitro LVV as it relates to all combinations of muscle layer input volume. The Endo, Trans, and Epi icons indicate which layers are active during each of the seven input combinations. If an icon is bolded, then it is active, and if it is faded, then it is inactive. (**E**) In vitro LV twist as it relates to all combinations of muscle layer input volume. (**F**) In vitro LV blocked-volume pressure, or pressure generation capabilities at a given internal LVV, as it relates to the sum of input volume to all layers of muscle. (**G**) In vitro peak blocked-volume LVP with respect to the blocked LVV with first-order line of best fit. (**H**) Input pressure versus volume for each artificial muscle layer.

There is also a brief notch in ventricular twist just as untwisting approaches completion in the filling phase, which matches well with data from Sengupta *et al.* (*43*), as seen in the second region highlighted in blue in both Figs. 4H and 4J. These idiosyncratic biological motions can be replicated and tuned through the bioinspired structure-input approach we have taken.

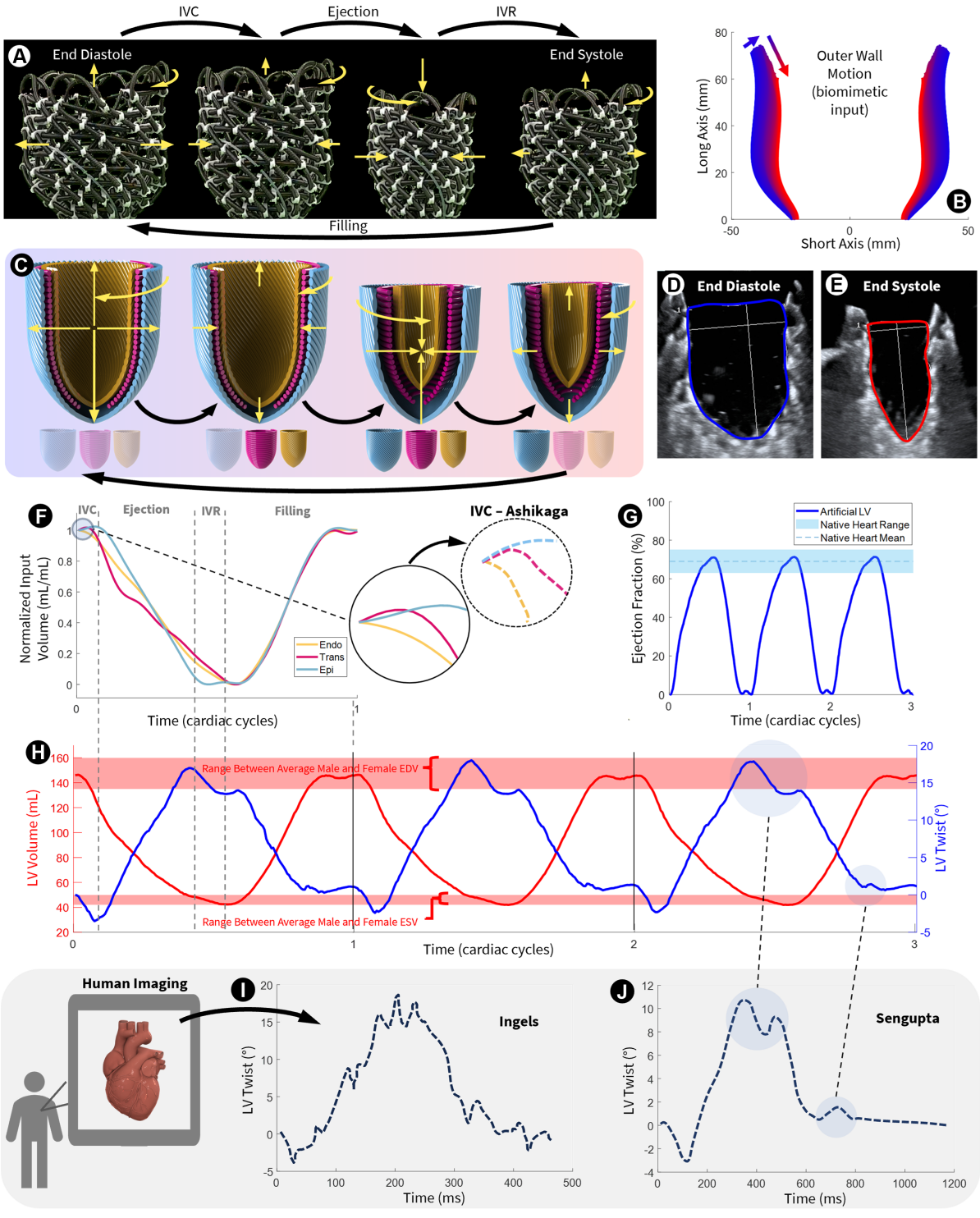

Fig. 4. Biomimetic input and motion analysis results. (**A**) Prototype motion with biomimetic input through the four phases of the cardiac cycle. (**B**) Outer surface motion of the LV from end diastole (blue) to end systole (red). (**C**) Human LV motion with a key indicating the active layers during each phase. (**D** and **E**) Ultrasound imaging of the LV inner surface at end diastole and end systole, respectively. (**F**) Normalized input volume to each muscle layer inspired by canine data from Ashikaga *et al.* (*39*). (**G**) EF over three cardiac cycles with the native heart's peak EF range and mean. (**H**) LVV and LV twist over three cardiac cycles. Overlaid are two red bands that correspond to the ranges of average male and female EDV (top) and ESV (bottom). (**I**) LV twist versus time data from Ingels *et al.* (*42*). (**J**) LV twist versus time data from Sengupta *et al.* (*43*).

In terms of volume characterization, Fig. 4G demonstrates very close agreement between the peak EF from our device and that of the physiological literature, with a peak EF of ~71% compared with a 69 ± 6% average (*44*). The instantaneous LVV data in Fig. 4H also reveal an EDV of ~146 ml and an ESV of ~42 ml compared with physiological averages of 160 ml (male)/135 ml (female) and 50 ml (male)/42 ml (female), respectively (*44*).

Given the simplifications in the design of our simulator and the use of canine strain data for control, this input signal needed to be tuned to reproduce the motion of a human LV. Thus, although the device is capable of a wide range of motions (figs. S2 to S7), we tuned our input signal to produce motion matching that of healthy hearts observed in the literature. Although these results were taken from an unloaded LV, through appropriate input tuning, such motions may be achievable.

As described in the Supplementary Materials, before physical experimentation, we applied this biomimetic input signal to our computational LV model to predict the motion of our physical prototype. Using the model as a predictive tool here aided us in the efficient construction of the biomimetic input signal. The comparison of those simulation results with subsequent prototype motion can be seen in fig. S8.

Mock circulation results

We then demonstrated the device's performance under physiologically relevant pressures using a simple MCL (Fig. 5A). The healthy LV pressure-volume (PV) loop in Fig. 5C shows that the device can replicate the four stages of the cardiac cycle, with four distinct phases in the loop. We also demonstrated our device's ability to simulate systolic dysfunction by limiting the contraction of the artificial muscles, mimicking decreasing inotropy or contractility. Figure 5 (B to E) reveals the results of this demonstration, with a decrease in SV and EF but an increase in both the EDV and ESV, paired with decreased end-systolic pressure (ESP) and increased end-diastolic pressure as inotropy was decreased. The "healthy" LV produced an ~69% EF with an SV of ~90 ml, and the first decrease in inotropy resulted in an EF of ~48%, putting this LV state in the heart failure with mid-range EF category (EF, 40 to 49%). The third case, with the largest reduction in inotropy, resulted in an ~28% EF, putting this LV state in the heart failure with reduced EF (HFrEF) category (EF, <40%).

We also investigated the effect of increasing the preload (filling pressure) on the LV's performance to see whether it has a natural, or passive, Starling response. With respect to the preload, the Frank-Starling law in a native heart describes the stretching of the myocardium to accommodate for increased venous return through increased diastolic filling pressure. This stretching of the myocardium then causes a stronger contraction during the following systole, increasing the SV. This law is one of the native heart's methods of autoregulation of cardiac output during periods of increased venous return, such as during exercise. From Fig. 5G, we can see that, when we increased the preload, there was an increase in EDV, which generated an increased SV and therefore an increased ESP. Unlike the native heart, the ESV remained constant for every increase in preload. This is evidence of the strength of our artificial muscles. Because we did not change the input to the muscle layers throughout this testing, the strength of our muscles brings the LV back to the same ESV after each ejection, no matter the ESP. Figure 5 (H and I) reveals the relationship of the EF and SV, respectively, to preload pressure. With an overall increase in preload of 12 mmHg, we saw a 14-ml increase in SV. Last, we tested the effect of increased afterload on the LV's SV (fig. S9). With a constant input actuation signal to the artificial muscles, we increased systemic arterial resistance in the MCL in incremental steps and observed a nonlinear decrease in SV with respect to end-diastolic aortic pressure (EDAOP) (the pressure required by the LV to open the aortic valve). This afterload sensitivity was small at normal EDAOPs (~80 mmHg) but became notable above 112 mmHg EDAOP. There was an 8-ml drop in SV (from 97 to 89 ml) when the EDAOP was increased from 78 to 112 mmHg. The SV then decreased a further 10 ml when the EDAOP was increased to 155 mmHg and decreased a further 18 ml when the EDAOP was increased to 191 mmHg. Although increasing the EDAOP above 120 mmHg is excessive, it was done to demonstrate the limitations of the muscles we used.

We then demonstrated our device's ability to assess the performance of a simple cardiac support device, the intra-aortic balloon pump (IABP). Figure 6A illustrates the IABP's integration into the mock loop. Figure 6B demonstrates the use of the IABP in the human body. This device is inflated during diastole to increase the systemic pressure and therefore perfusion in the coronary arteries, delivering more oxygen to cardiac tissue. The subsequent rapid deflation of the IABP causes a suction event that reduces the AOP before the next systole. This reduction in EDAOP or afterload gives relief to the heart, making pumping easier (producing a reduction in ESP) and reducing its myocardial oxygen demand. Figure 6D shows the IABP's operation within our mock loop through a simple syringe pump. Figure 6C reveals the pressure data from our mock loop before, during, and after IABP operation. Before operation, both the ESP and EDAOP were constant at ~133 and ~81 mmHg, respectively. We then actuated the IABP a total of four times (seen in AOP during the green region). This resulted in a reduction in ESP and EDAOP of ~8 and ~12 mmHg, respectively, as highlighted in Fig. 6 (E and F) and then returned to its original state upon cessation of IABP intervention. This reduction in both ESP and EDAOP is indicative of the expected IABP performance and evidences our device's ability to conduct in vitro simulations on cardiac support devices.

Predicting LV motion with changing the helix angle and cardiac geometry and strain

Last, we used the COMSOL model of our artificial LV to investigate the predicted effects of adjusting the helix angles of the fibers in the Endo and Epi layers on LV motion. We also combined this with changes to LV geometry and changes to the strain applied to the fibers in each layer. Our model's ability to change these parameters gives us predictive power over the LV device's function when designed to simulate various cardiomyopathic states, such as dilated cardiomyopathy (DCM) and HFrEF. Patients with DCM have an enlarged, weakened LV (*45*), meaning a reduced SV and reduced supply of oxygen to bodily tissues. This gradual dilation of the ventricle is caused by geometric remodeling of the myocardium, which becomes more spherical as remodeling progresses, and the wall thickness of the myocardium also reduces. The result is a ventricle with a greater sphericity index and reduced contractility. The fiber helix angles in each layer of the myocardium also change with geometry during this process. Although there is debate over the orientation of these angle changes, recent studies suggest that a large proportion of the fibers in both the Endo and Epi layers become steeper (*46*–*48*).

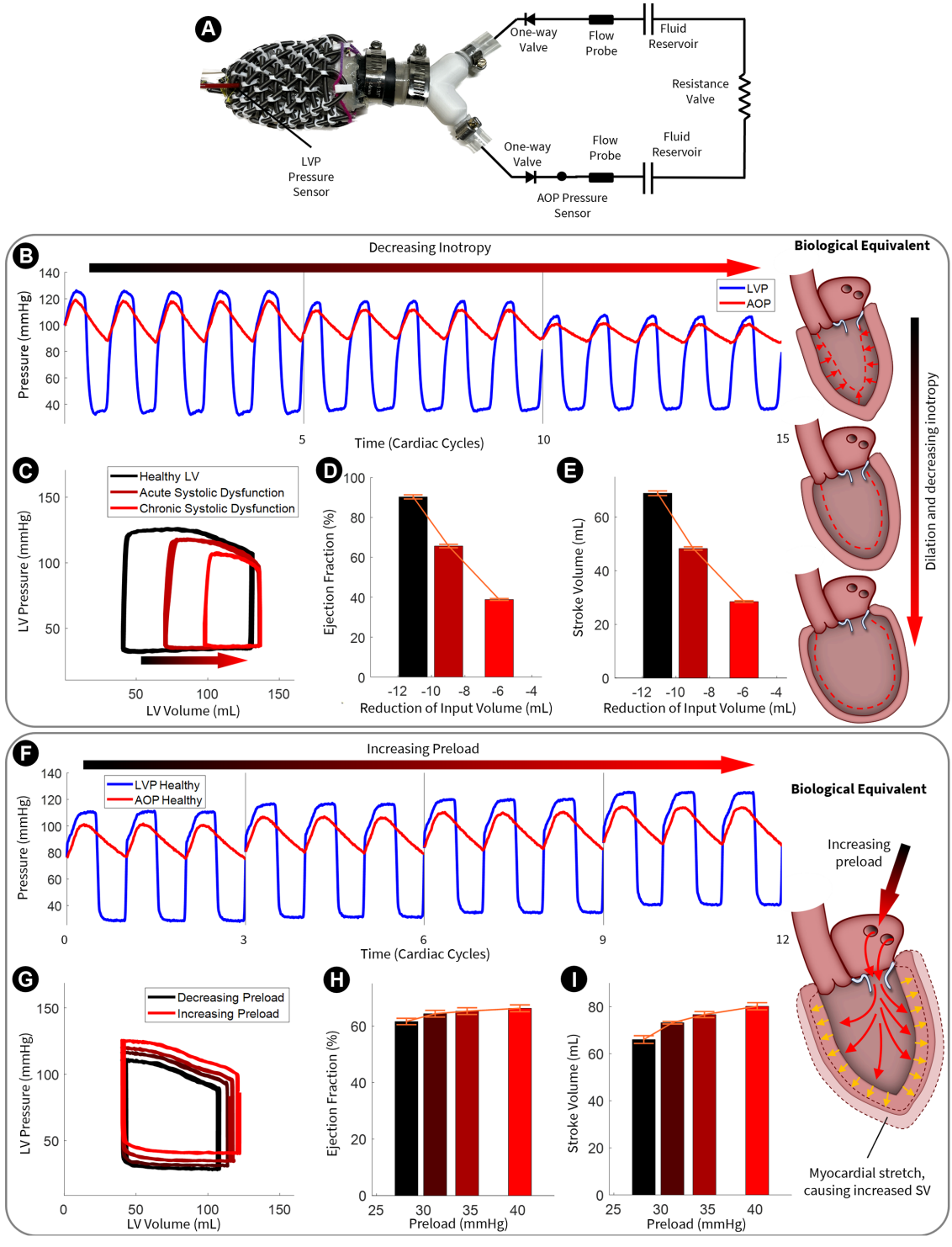

Fig. 5. MCL simulation results. (**A**) Circuit diagram to represent the loop used in these simulations. (**B**) LVP and AOP over three groups of five cardiac cycles each with decreasing inotropy. (**C**) LVP versus LVV loops for each of the three groups of decreasing inotropy. (**D**) EF for each group. (**E**) SV for each group. (**F**) LVP and AOP over four groups of three cardiac cycles each with increasing preload. (**G**) LVP versus LVV loops for each group of increasing preload. (**H**) EF for each group. (**I**) SV for each group. All error bars represent 1 SD.

Our in silico model of the artificial LV can be used to predict the effects of changing various design and actuation parameters. These can include ventricular geometry, muscle layer strain, and the fiber angle of each muscle layer. Figure 7A visualizes changes in the fiber helix angles of each muscle layer. We modeled Endo/Epi angle pairs of ±0° to ±90° for all scenarios at 10° increments. We

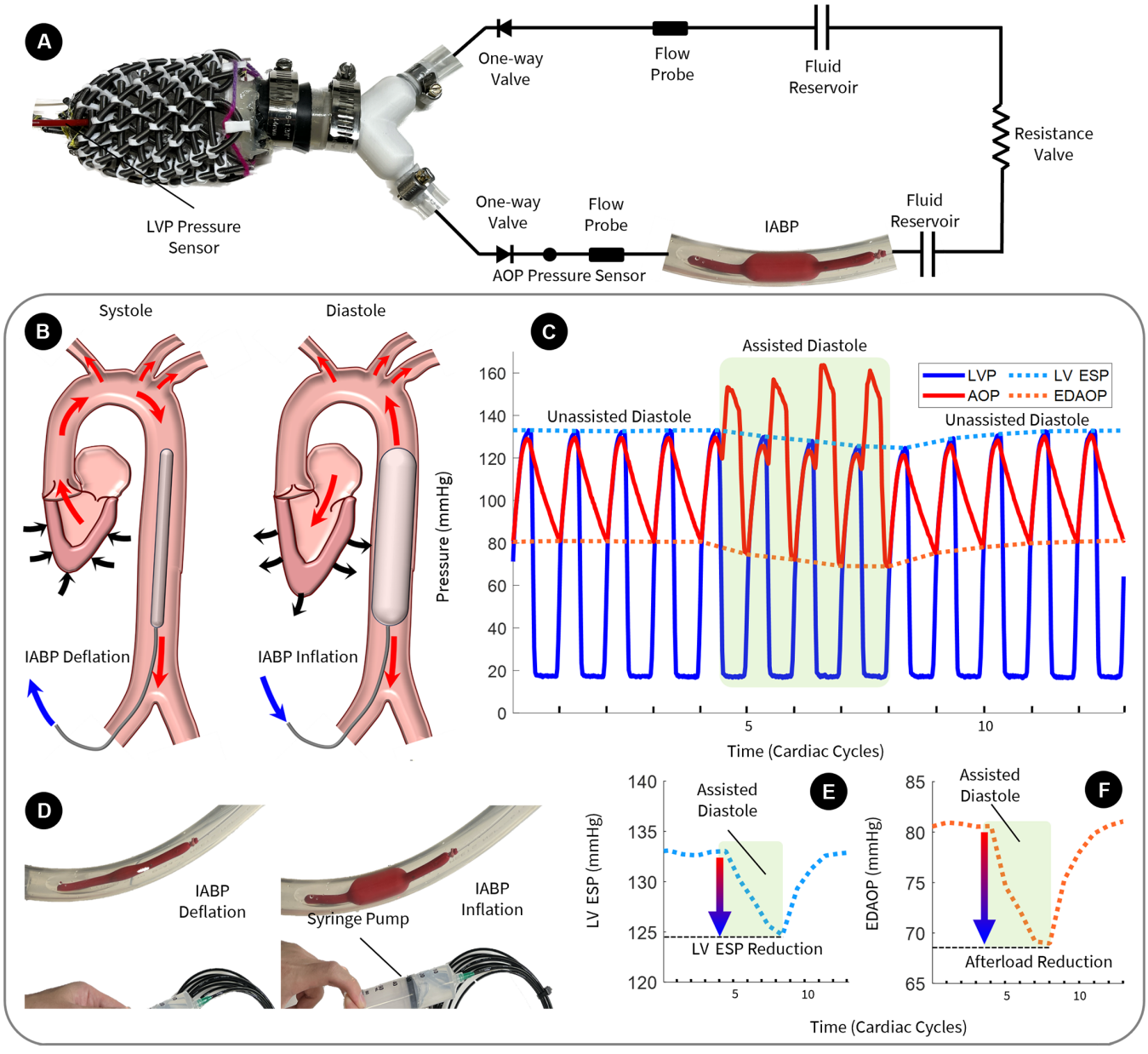

Fig. 6. Simulation of a simple IABP. (**A**) Circuit diagram to represent the MCL used in this simulation, with an implanted IABP. (**B**) Demonstration of the operation of IABPs within the human body. (**C**) Pressure data from the MCL before, during, and after IABP operation. (**D**) Operation of the IABP within the MCL during testing. (**E** and **F**) LV ESP and EDAOP before, during, and after IABP operation, respectively.

also investigated changes in LV geometry and muscle layer strain, as shown in Fig. 7B.

Figure 7 (C to K) includes data from four different LV states: healthy geometry with healthy layer strains, healthy geometry with diseased layer strains, dilated geometry with healthy layer strains, and lastly dilated geometry with diseased layer strains. The first case represents a healthy heart, whereas the last case represents a heart with DCM. Diseased layer strain simply means a reduction in contraction strain applied to each layer of the myocardium by 60% compared with healthy strain, as detailed in Fig. 7B. We investigated changes in LV height, diameter, twist, and volume for each LV state case with all Endo/Epi helix angle pairs. More details can be found in fig. S10.

Figure 7 (C and D) reveals that, in all cases, there was a general trend toward greater shortening of the LV as the helix angle increased in steepness. Both healthy strain input cases (for healthy and dilated geometry) were closely related. Similarly, both diseased strain input cases (for healthy and dilated geometry) were also closely related. This coupling suggests that contraction strain was a main driver of height change when compared with LV geometry or sphericity. Naturally, greater layer contraction strains amplified the height change and seem to be the dominant factor when compared with the helix angle. These trends were replicated for both the LV diameter change and twist, as shown in Fig. 7 (E to H). Here, greater contraction produced greater diameter change and twist, almost independent of LV geometry.

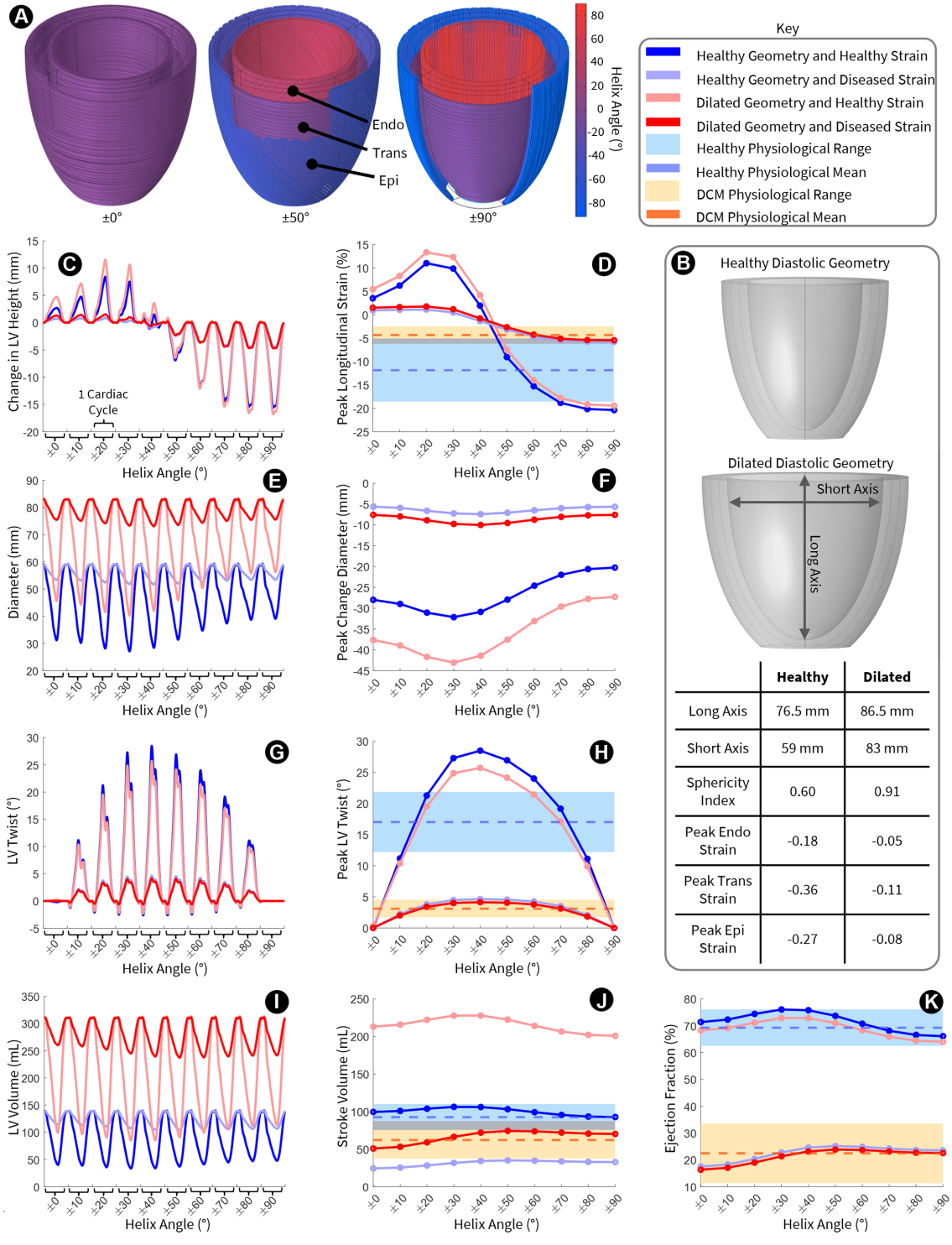

	Healthy	Dilated
Long Axis	76.5 mm	86.5 mm
Short Axis	59 mm	83 mm
Sphericity Index	0.60	0.91
Peak Endo Strain	-0.18	-0.05
Peak Trans Strain	-0.36	-0.11
Peak Epi Strain	-0.27	-0.08

Fig. 7. Modeling of LV motion with varying myocardial layer helix angle and cardiac geometry. (**A**) Visualization of muscle fiber angles in simulated artificial LV. (**B**) Visualization of healthy and dilated LV geometry used in this modeling, accompanied by a table describing the short- and long-axis dimensions, along with the peak strains applied to muscle fibers in each layer for both geometries. (**C**) Change in height through one cardiac cycle for Endo and Epi helix angles from ±0° to ±90°. (**D**) Peak change in height during the cardiac cycle with respect to the helix angle. (**E**) Change in diameter through one cardiac cycle. (**F**) Peak change in diameter during the cardiac cycle with respect to the helix angle. (**G**) Change in twist through one cardiac cycle. (**H**) Peak change in twist during the cardiac cycle with respect to the helix angle. (**I**) Change in volume through one cardiac cycle. (**J**) Peak change in SV during the cardiac cycle with respect to the helix angle. (**K**) Peak change in EF during the cardiac cycle with respect to the helix angle.

For all cases, although helix steepening generally resulted in a decrease in diameter change, LV twist peaked at an approximately ±40° helix angle and dropped off as the helix angle increased or decreased from this point. Figure 7 (I and J) shows that the change in volume of the LV was dependent on both contraction strain and geometry. Reduced contraction strain naturally reduced volume change, and dilated initial diastolic geometry amplified volume change for any level of strain. The SV for cases with healthy strain was negatively affected by increasing the helix angle and positively affected in cases with diseased strain. When looking at the EF (Fig. 7K), we saw the same coupling between cases with the same contraction strain, regardless of geometry. There was also a general decrease in EF with increasing the helix angle for cases with healthy strain, and the opposite was true for cases with diseased strain.

Both the healthy geometry/strain and dilated/diseased geometry/strain cases showed good agreement with the literature in terms of volume and EF. This agreement can be seen in Table 1, where modeling predictions are given against observed physiological values. Where large/healthy strain was applied, LV twist was very sensitive to the helix angle, and as can be seen in fig. S8C, our model slightly overpredicted LV twist when compared with the physical device. This overprediction was likely due to differences in the mechanics between the model and the device because simplifications were necessary. The same overprediction can be seen in Table 1, where the peak twist of the device was modeled with healthy strain, geometry, and helix angles and compared with physiological values. However, this healthy physiological range is much wider than the reported physiological DCM LV twist range (*49*) (Fig. 7H and Table 1). This could suggest that the same simulated twist sensitivity to fiber angle with large/healthy contraction strain exists in the native heart. We also saw a similar longitudinal strain sensitivity to helix fiber angle where large/healthy contraction strain was applied in Fig. 7D. Again, here, the physiological range is wide in the healthy case and narrow in the DCM case, as shown in Fig. 7D and Table 1. Good agreement with physiological observations of longitudinal strain in the healthy LV case with ±60° fiber angles can be seen in Fig. 7D and Table 1. The longitudinal strain data for our DCM case matched well with physiological observations of helix fiber angles from ±50° to ±90° (Fig. 7D and Table 1), which could help to support recent suggestions that a greater proportion of steep fiber angles exist in hearts with DCM. LV longitudinal strain may hold more weight clinically than other parameters because it may be a particularly good prognostic indicator of DCM and recovery (*50*).

DISCUSSION

In this work, we introduce a method for the design, fabrication, and control of a biomimetic artificial LV, which has the potential to be used as a high-fidelity benchtop simulator for in vitro cardiac device testing and surgical training. Current simulators, both ex vivo and soft robotic, are not able to fully recapitulate cardiac motion, especially not while maintaining hemodynamic performance. Here, we present an artificial left ventricular musculature that can produce both biomimetic motion and physiological PV performance. We also demonstrate the device's ability to simulate varying degrees of systolic dysfunction consistent with systolic LV heart failure.

We used a three-layer simplification of the continuous fiber model of the heart, replicating the Endo, Trans, and Epi layers using an artificial myocardial muscle analog. This cardiac simulator uses these hydraulically driven inverse PAMS, with other devices having relied on positive pressure PAMs. We believe that our choice of actuation is the key to achieving the unmatched biomimetic motion we have reported, even down to small idiosyncratic torsional motions that have been observed in the literature. This choice of actuation allowed close physical adherence to the continuous fiber model of the heart, the most widely accepted myocardial model. The combination of appropriate actuators and biomimetic structure, paired with biomimetic input signals, necessitates biomimetic motion. In the case of this device, we mimicked the structure of a healthy heart and gave it a healthy input signal. However, our design approach has the potential to facilitate patient-specific or disease-specific muscle fiber arrangements. Pairing this with patient-specific or disease-specific fiber strain input could allow for specific simulations for training, research, or device testing. The biomimetic motion analysis results we have presented indicate the potential for the device's use in applications where high-fidelity simulation is essential for positive outcomes, including surgical procedure training and cardiac device development.

We integrated this artificial LV, with its biomimetic input, into a simple left-sided MCL to demonstrate its ability to mimic physiological hemodynamic performance. The device was able to pump against physiological pressures with an appropriate SV and EF. We were also able to demonstrate its ability to limit contraction to simulate systolic dysfunction to varying degrees. This demonstrates the device's potential to simulate varying disease-specific or patient-specific conditions for diverse purposes, including in vitro cardiac device development.

One of the most obvious limitations for the device in its current form is the lack of myocardial wall thickening upon contraction because of the current fabrication process. This constant-thickness LV

Table 1. Comparison of device motion predictions and physiological observations.

	Healthy geometry and strain		Diseased geometry and strain	
Metric	**Device prediction**	**Native LV**	**Device prediction**	**Native LV**
EDV (ml)	140	133.6 ± 12.6 (*45*)	307	298.4 ± 128.8 (*45*)
SV (ml)	93 to 106*	92.5 ± 17.3 (*45*)	51 to 74*	62.1 ± 25.1 (*45*)
EF (%)	66 to 76*	69.3 ± 6.8 (*45*)	16 to 24*	22.4 ± 11.1 (*45*)
Peak twist (°)	24.6†	17.0 ± 4.8 (*54*)	0 to 4*	3.1 ± 1.4 (*49*)
Longitudinal strain (%)	−15†	−11.9 ± 6.8 (*45*)	−5 to 2*	−4.3 ± 1.8 (*45*)

*Depending on the helix angle. †Endo/Epi helix angles at ±60°.

wall dictates that the outer surface of the device must move in the same way as the inner surface to achieve the appropriate volumetric performance. Native cardiac muscle fibers thicken upon contraction, which means that they can create a greater level of LV chamber volume change (~69%) with relatively little fiber strain [<20% (*51*)]. The native heart's outer surface volume only reduces by 8% during systole (*52*). In the future, we aim to integrate our muscle fibers into an incompressible matrix, like the native heart's ECM (*31*), which will allow wall thickening and potentially close to 100% biomimetic motion. Such a compliant stabilizing structure would not only reduce the necessary operating strain of our muscle fibers but also provide the additional compliance that our device currently lacks. We also plan for this ECM to include the internal and external biological structures that our current musculature omits to increase its suitability for the simulation of surgical procedures. The Starling response results, while promising, are perhaps less sensitive to the preload than biological examples. Currently, this increase in SV with increasing preload is made possible by the slight stretchability of the thin blood-contacting membrane that lines the musculature. If this membrane was replaced by a more compliant ECM tissue surrounding the muscle fibers, then this Starling response would likely be amplified. The Starling response results also revealed the nonbiomimetic behavior of a constant ESV with increasing ESP. However, with this occurring because of the strength of our muscles, we believe that we may be able to directly tune and control the increase in ESV in response to ESP. In the native heart, this relationship is indicative of its contractile state. Our device could potentially include this as a control parameter.

Another limitation of this research lies in the speed of actuation applied to the artificial myocardium during characterization. This is not a limitation of the artificial muscles used but of the actuation system used to drive them. At the time of characterization, our available hydraulic pumping equipment did not have the power to drive the system at a high speed. We therefore characterized the device at about 1 beat per minute (bpm), which allowed high-resolution motion and performance analysis. We have since begun work to develop a more powerful drive system and used it to demonstrate device actuation at 30 bpm (see movie S1). Future work will include further optimization of the drive system to allow actuation exceeding 60 bpm. Although this actuation speed may affect the system's utility for certain applications, our simple IABP demonstration suggests that it may be possible to assess certain circulatory support device working principles, including those at the first stages of development, at slow actuation speeds. That being said, apart from drive system improvements, there are adjustments that can be made to the muscles used in our system to help approach faster speeds. These include using more, shorter-diameter, and/or larger-diameter muscle fibers, which offer less resistance to hydraulic input and therefore less cavitation potential. As seen in fig. S11, we used long meandered muscles to form the various helices, and these can be divided into shorter individual fibers. Although this paper serves as a proof of concept for the design, fabrication, and control of a biomimetic artificial LV, future work will be directed at improving its clinical utility, including actuation speed.

Our developed computational model of the device also offers us predictive power in the investigation of altered design parameters. For example, we can potentially use it to predict the motion of a failing heart whose ventricular musculature has been remodeled. All of these geometric parameters, combined with altered muscle activation, can be simulated using this model, all before a physical prototype has been fabricated. This was demonstrated in the previous section. Furthermore, our model has the capability to include wall thickening, as described above. Therefore, we can potentially model this future device development and use it to inform design choices. This will be an important tool to speed progress toward 100% biomimetic motion.

Along with these limitations, it is important to note the possibility of the addition of more muscle fiber layers (±30° fibers, for example). The continuum model and recent cardiac imaging suggest the existence of a continuum of incremental fiber angles across the myocardial wall. Although our simplification of this model to three fiber layers is sufficient to replicate cardiac motions, it necessitates tuning the measured biological strain data of the heart to achieve the precise measured range of motion. Although this tuning process is straightforward because of the simplicity of our device, less tuning would be required with a more anatomically accurate model. In other words, the closer our model is to the native heart, the easier it becomes to directly use biological strain measurements for control.

We are also encouraged by continued advances in multimaterial additive manufacturing, which will improve the speed and reliability of the fabrication of our LV device. The current fabrication method is very hands-on and requires some skill, which is sufficient for small-scale production but needs to be improved to reach the scale required by the industry. For example, Buchner *et al.* (*53*) have introduced a method of 3D-printing complex multimaterial soft robotic structures, which could be adopted here to materialize the entire passive LV structure, with its supportive pins, membrane, and valves, leaving only the manual insertion of the artificial muscles. Our work in this paper serves as a proof of concept for the design, fabrication, and control of a biomimetic artificial LV, and in combination with advances in additive manufacturing, this could make for reliable, fast, patient-specific device construction.

Our biomimetic artificial LV musculature, with its biomimetic input, has the potential to be used as a high-fidelity cardiac simulator, replacing early ex vivo and in vivo testing of surgical procedures and cardiac assist devices. These ex vivo and in vivo trials are time-consuming and expensive, and biological models have a limited lifetime. The device may also be able to provide a wide range of functional and dysfunctional states, including the integration of patient-specific data. There is also potential to extend this device to include a right ventricle, designed and actuated in the same biomimetic manner, which would aid in simulating the complex interplay between left and right ventricular function, especially under MCS. With the future developments discussed above, this device has the potential to become a truly biomimetic, tunable left ventricular model.

MATERIALS AND METHODS

Fabrication and control of the left ventricular musculature

For the purposes of this paper, we set the Epi and Endo fiber angles to those of a typical healthy human heart (±60°) and set the Trans fiber angle to ~0°. These fiber angles were programmed into a 3D-printed pinboard (Prusa MK3S+, Prusa Research; PolyMax PLA, Polymaker) and its associated pins. Holes were printed into the pinboard to accept the 3D-printed pins (Prusa MK3S+, Prusa Research; PolyMax PLA, Polymaker) at the desired fiber density and angle. Here, we used a simplified bullet shape as the morphology of the pinboard, which represents the end-systolic LV chamber dimensions (diameter of 34 mm; length of 60 mm), but this shape can be altered to simulate failing, remodeled ventricles. After manually inserting

the pins into the pinboard, we manually threaded long HFAM fibers through the holes in the pins. We started with the bottom Endo layer before threading the Trans layer and lastly the outer Epi layer. We then fixed the ends of the muscle fibers and the joints between the muscle fibers and the pins with cyanoacrylate (UHU GmbH & Co. KG) before pressurizing the muscles, which expanded the artificial LV, allowing the removal of the pinboard. This process is also visualized in movie S6. At this stage, the pin shafts were trimmed, leaving only the pin bodies, which stabilized the muscle fibers in the desired orientations, completing the artificial LV musculature (fig. S12). Further details on the fabrication of the device and its musculature, control, and actuation can be seen in fig. S11. Here, we show that each layer of the muscle consisted of two individual, long muscle fibers, which were both connected to the same hydraulic piston pump via a shared fluid transmission line. For each of the three layers, the two constituent muscle fibers were of equal lengths (fig. S11), meaning that they each shared half of the input volume from the piston pump.

Each muscle layer was formed using HFAM muscles (*28*) consisting of natural latex rubber inner tubes [1.6-mm inner diameter (ID), 3.2-mm outer diameter (OD), Uxcell] and external spring coils [36 inches (91.44 cm) long, 0.125-inch (0.3175-cm) OD, 0.014-inch (0.0356-cm) wire diameter, spring constant of 0.02 psi (137.9 Pa), McMaster-Carr]. Material properties of the components used within the LV device can be found in Table 2. More details of material properties can be found in fig. S13.

The actuation of each layer was controlled using DC (direct current) motor-controlled syringe pumps (BD Luer-Lok). Using a QPIDe Data Acquisition Device (QUANSER, Canada) and MATLAB Simulink (MathWorks Inc., United States), we devised a closed loop controller, which applied the periodic basic or biomimetic inputs with adjustable amplitude, frequency, and phase. The average power consumption at 30 bpm for the Epi, Trans, and Endo layers during actuation was 34, 32, and 34 W, respectively (Epi and Endo power draw was estimated to be equal). This equated to an average power consumption of 100 W for the entire system, which is equivalent to 0.1 kilowatt-hour. The power and current draw for the Epi and Trans layers can be seen in fig. S14.

Range of motion and biomimetic motion analysis

Both the range of motion and biomimetic motion analyses were performed using image processing through the image processing and computer vision toolbox in MATLAB. We extracted the short-long axes plane motion by placing a greenscreen behind our prototype (with its apex fixed and base free to move) and capturing a front-view video (fig. S15). Through thresholding, we recorded the silhouette of the device as it moved because of our input signal. We used a visual marker to track the effective height of the LV for volume and shape calculations. Assuming axisymmetric movement, we tracked one edge of the LV, rotating this around its axis of symmetry (found by calculating the centroid of the LV silhouette) for volume and shape calculations. To extrapolate from the outer surface motion to the inner surface ("blood-contacting" surface), we subtracted the length of the rigid 3D-printed pins (13.4 mm) that form the thickness of the LV wall. This assumption of constant wall thickness is reasonable under the unloaded conditions of this motion analysis. To extract the LV twist data, we placed a visual marker across the top surface of the LV and recorded a top-view video as the device moved because of our input signal (fig. S15). Through thresholding, we measured the angle of this marker through the cardiac cycle.

For the range of motion testing, we performed motion analysis for every permutation of muscle layer contractions. We set the diastolic state of the LV by inputting ~3 ml into both the Epi and Endo muscle layers and inputting ~2.75 ml into the Trans layer. Then, for every permutation of layer contractions, we withdrew all this volume at peak systole and inputted it again at peak diastole in a sinusoidal manner. This sinusoidal contraction and dilation completed one cardiac cycle. For each permutation of layer contraction, we performed three cardiac cycles ($n = 3$).

For the biomimetic motion testing, we set the diastolic state of the LV by inputting ~4.11, ~4.11, and ~3.43 ml into the Endo, Epi, and Trans layers, respectively. We then applied the contraction of these layers by withdrawing water according to the biomimetic periodic function we reconstructed from the canine heart strain data. We set the amplitude of contraction to withdraw ~2.11, ~2.94, and ~2.86 ml from the Endo, Epi, and Trans layers, respectively. This input signal is visualized in fig. S16. We conducted motion testing on three cardiac cycles ($n = 3$).

Mock circulation loop

For both the inotropy and Starling testing, the MCL (fig. S17) was set up such that two fluid reservoirs, or fluid columns, and their fluid levels controlled both the AOP and the LV filling pressure. Water was pumped out of the LV, raising the water level in the small-diameter outlet reservoir (10-mm ID), thus raising the AOP. This drained into a large-diameter LV inlet reservoir (meaning a near-constant water level) [6-inch (15.24-cm) standard wall clear polyvinyl chloride (PVC) pipe, McMaster-Carr], which controlled the filling pressure of the LV. Both fluid columns were supported by adjustable-height aluminum frames and connected by soft tubing [7/8-inch (2.22-cm) ID, 1- and 1/8-inch (2.86-cm) OD, Tygon PVC soft plastic tubing, McMaster-Carr] to each other and to the LV. An ultrasonic flow meter was placed in series with the inlet of the LV and another at the outlet (Atrato Series Ultrasonic Flow Meter, 0.1 to 20 liter/min, Atrato). A 3D-printed aperture (Prusa MK3S+, Prusa Research;

Table 2. Material properties of components used in the device. N/A, not applicable.

Component	Elastic modulus	Shear modulus	Burst pressure/failure
Artificial muscle	0.96 MPa @ 60%	N/A	1.88 MPa
Inner tube	0.62 MPa @ 60%	0.22 MPa	0.39 MPa
Outer coil	0.02 pounds/inch (0.0069 MPa) for a 1-inch (2.54-cm) segment	N/A	N/A
LV inner membrane	132 MPa @ 5%	N/A	N/A

PolyMax PLA, Polymaker) was fixed to a polyethylene bag, which formed the blood-contacting membrane within the artificial musculature. A fluid transmission line was then integrated into the bag and attached to a pressure sensor (40PC Series Sensor, Honeywell, United States), which monitored the ventricular pressure. This aperture was then fixed to the artificial musculature such that the bag was inside the musculature. The outlet to the aperture was bifurcated, with each opening fixed to a one-way valve, forming an inlet and an outlet to the LV chamber. At the LV outlet, past the outlet valve, another fluid transmission line was then integrated into the tubing, which monitored the effective AOP (40PC Series Sensor, Honeywell, United States). A resistance valve was placed between the outlet of the aortic fluid column and the inlet of the atrial filling reservoir to control the draining rate from the aortic fluid column, ensuring no accumulation over consecutive cardiac cycles.

The data from the pressure sensors were decoded by a QPIDe Data Acquisition Device (QUANSER, Canada) and MATLAB Simulink (MathWorks Inc., United States), and the flow meter data were read using Atrato's proprietary software. To synchronize these two data acquisition methods, we used index events where both the pressure and flow were altered simultaneously. The flow data were resampled to match those of the pressure data using MATLAB.

For the inotropy testing, we set the healthy diastolic state of the LV by inputting 4.12 ml of water into both the Epi and Endo muscle layers and 2.85 ml into the Trans layer. We then set the biomimetic input volume functions such that they withdrew all this volume from the muscles at peak systole. For the first decrease in inotropy, we set the diastolic state of the LV by inputting 4.12 ml of water into both the Epi and Endo muscle layers and 4 ml into the Trans layer. We then withdrew 3.06 ml from both the Epi and Endo muscle layers and 2.86 ml from the Trans layer at peak systole. For the second decrease in inotropy, we set the diastolic state of the LV by inputting 4.12 ml of water into both the Epi and Endo muscle layers and 3.43 ml into the Trans layer. We then withdrew 2.12 ml from both the Epi and Endo muscle layers and 1.71 ml from the Trans layer at peak systole. For each decrease in inotropy, we ran five cardiac cycles ($n = 5$).

For the preload/Starling response testing, we set an arbitrary diastolic state of the LV by inputting 4.12 ml of water into both the Epi and Endo muscle layers and 3.2 ml into the Trans layer. We then set the biomimetic input volume functions such that they withdrew all this volume from the muscles at peak systole. For the first preload test, we set the filling pressure to 28.17 mmHg. For the second, third, and fourth preload tests, we set the filling pressure to 31.20, 34.58, and 40.17 mmHg, respectively. For each trial, we ran three cardiac cycles ($n = 3$). The afterload sensitivity testing (fig. S9) was done using the same LV control signal as above but varying the systemic arterial resistance and keeping the arterial compliance and preload constant. Initially, the resistance was set low, producing an EDAOP of 78 mmHg, and the SV over nine cardiac cycles was recorded. We then increased the resistance three more times to produce EDAOPs of 112, 155, and 191 mmHg and recorded the SV over nine, four, and four cardiac cycles, respectively.

The IABP and afterload testing was conducted using the same LV control parameters as above but using the MCL, as shown in fig. S18. This MCL differs from the one outlined above in that it uses compliance chambers and resistance valves to build and dissipate the pressure. These compliance and resistance values were determined experimentally to achieve the desired output.

Statistical analysis

The linear fitting in Fig. 3G and fig. S13E was calculated and plotted using MATLAB and its curve fitting toolbox. The SDs and subsequent error bars in Fig. 5 (D, E, H, and I) were calculated using $n = 5$ and $n = 3$, respectively. The nonlinear fitting in fig. S9B was calculated and plotted using MATLAB and its curve fitting toolbox. The SDs and subsequent error bars in fig. S9B were calculated using $n = 9$, $n = 9$, $n = 4$, and $n = 4$, from left to right, respectively.

Supplementary Materials

The PDF file includes:

Discussion
Methods
Figs. S1 to S18
Tables S1 and S2
References (*55*–*69*)

Other Supplementary Material for this manuscript includes the following:

Movies S1 to S6

REFERENCES AND NOTES

1. S. Maglio, C. Park, S. Tognarelli, A. Menciassi, E. Roche, High-fidelity physical organ simulators: From artificial to bio-hybrid solutions. *IEEE Trans. Med. Robot. Bionics* **3**, 349–361 (2021).
2. N. J. Maran, R. J. Glavin, Low-to high-fidelity simulation—A continuum of medical education? *Med. Educ.* **37**, 22–28 (2003).
3. A. K. Lefor, K. Harada, H. Kawahira, M. Mitsuishi, The effect of simulator fidelity on procedure skill training: A literature review. *Int. J. Med. Educ.* **11**, 97–106 (2020).
4. A. Bakhsh, G. F. Martin, C. D. Bicknell, C. Pettengell, C. Riga, An evaluation of the impact of high-fidelity endovascular simulation on surgeon stress and technical performance. *J. Surg. Educ.* **76**, 864–871 (2019).
5. L. J. Olivieri, L. Su, C. F. Hynes, A. Krieger, F. A. Alfares, K. Ramakrishnan, D. Zurakowski, M. B. Marshall, P. C. W. Kim, R. A. Jonas, D. S. Nath, "Just-in-time" simulation training using 3-D printed cardiac models after congenital cardiac surgery. *World J. Pediatr. Congenit. Heart Surg.* **7**, 164–168 (2016).
6. J. P. Costello, L. J. Olivieri, L. Su, A. Krieger, F. Alfares, O. Thabit, M. B. Marshall, S. J. Yoo, P. C. Kim, R. A. Jonas, D. S. Nath, Incorporating three-dimensional printing into a simulation-based congenital heart disease and critical care training curriculum for resident physicians. *Congenit. Heart Dis.* **10**, 185–190 (2015).
7. E. Chinchoy, C. L. Soule, A. J. Houlton, W. J. Gallagher, M. A. Hjelle, T. G. Laske, J. Morissette, P. A. Iaizzo, Isolated four-chamber working swine heart model. *Ann. Thorac. Surg.* **70**, 1607–1614 (2000).
8. J. McHale, F. F. Fago, M. Monti, R. M. Trusty, J. Wesley, J. P. Sites, E. S. Norman, US Patent 20210272482A1 (2021).
9. P. S. Ramphal, D. N. Coore, M. P. Craven, N. F. Forbes, S. M. Newman, A. A. Coye, S. G. Little, B. C. Silvera, A high fidelity tissue-based cardiac surgical simulator. *Eur. J. Cardiothorac. Surg.* **27**, 910–916 (2005).
10. A. Leopaldi, R. Vismara, S. van Tuijl, A. Redaelli, F. N. van de Vosse, G. B. Fiore, M. C. M. Rutten, A novel passive left heart platform for device testing and research. *Med. Eng. Phys.* **37**, 361–366 (2015).
11. R. Vismara, A. M. Leopaldi, M. Piola, C. Asselta, M. Lemma, C. Antona, A. Redaelli, F. van de Vosse, M. Rutten, G. B. Fiore, In vitro assessment of mitral valve function in cyclically pressurized porcine hearts. *Med. Eng. Phys.* **38**, 346–353 (2016).
12. A. L. Richards, R. C. Cook, G. Bolotin, G. D. Buckner, A dynamic heart system to facilitate the development of mitral valve repair techniques. *Ann. Biomed. Eng.* **37**, 651–660 (2009).
13. A. M. Leopaldi, K. Wrobel, G. Speziali, S. van Tuijl, A. Drasutiene, W. R. Chitwood Jr., The dynamic cardiac biosimulator: A method for training physicians in beating-heart mitral valve repair procedures. *J. Thorac. Cardiovasc. Surg.* **155**, 147–155 (2018).
14. E. T. Roche, R. Wohlfarth, J. T. B. Overvelde, N. V. Vasilyev, F. A. Pigula, D. J. Mooney, K. Bertoldi, C. J. Walsh, A bioinspired soft actuated material. *Adv. Mater.* **26**, 1200–1206 (2014).
15. E. T. Roche, M. A. Horvath, I. Wamala, A. Alazmani, S.-E. Song, W. Whyte, Z. Machaidze, C. J. Payne, J. C. Weaver, G. Fishbein, J. Kuebler, N. V. Vasilyev, D. J. Mooney, F. A. Pigula, C. J. Walsh, Soft robotic sleeve supports heart function. *Sci. Transl. Med.* **9**, eaaf3925 (2017).
16. C. Park, C. Ozturk, E. T. Roche, Computational design of a soft robotic myocardium for biomimetic motion and function. *Adv. Funct. Mater.* **5**, 2206734 (2022).
17. M. Carlsson, M. Ugander, H. Mosén, T. Buhre, H. Arheden, Atrioventricular plane displacement is the major contributor to left ventricular pumping in healthy adults,

athletes, and patients with dilated cardiomyopathy. *Am. J. Physiol. Heart Circ. Physiol.* **292**, H1452–H1459 (2007).
18. C. Park, Y. Fan, G. Hager, H. Yuk, M. Singh, A. Rojas, A. Hameed, M. Saeed, N. V. Vasilyev, T. W. J. Steele, X. Zhao, C. T. Nguyen, E. T. Roche, An organosynthetic dynamic heart model with enhanced biomimicry guided by cardiac diffusion tensor imaging. *Sci. Robot.* **5**, eaay9106 (2020).
19. D. H. MacIver, J. B. Partridge, P. Agger, R. S. Stephenson, B. J. D. Boukens, C. Omann, J. C. Jarvis, H. Zhang, The end of the unique myocardial band: Part II. Clinical and functional considerations. *Eur. J. Cardiothorac. Surg.* **53**, 120–128 (2018).
20. D. H. MacIver, R. S. Stephenson, B. Jensen, P. Agger, D. Sánchez-Quintana, J. C. Jarvis, J. B. Partridge, R. H. Anderson, The end of the unique myocardial band: Part I. Anatomical considerations. *Eur. J. Cardiothorac. Surg.* **53**, 112–119 (2018).
21. J. I. Hoffman, Will the real ventricular architecture please stand up? *Physiol. Rep.* **5**, e13404 (2017).
22. C. Park, M. Singh, M. Y. Saeed, C. T. Nguyen, E. T. Roche, Biorobotic hybrid heart as a benchtop cardiac mitral valve simulator. *Device* **2**, 100217 (2024).
23. M. Singh, J. Bonnemain, C. Ozturk, B. Ayers, M. Y. Saeed, D. Quevedo-Moreno, M. Rowlett, C. Park, Y. Fan, C. T. Nguyen, E. T. Roche, Robotic right ventricle is a biohybrid platform that simulates right ventricular function in (patho)physiological conditions and intervention. *Nat. Cardiovasc. Res.* **2**, 1310–1326 (2023).
24. G. Buckberg, J. I. Hoffman, Right ventricular architecture responsible for mechanical performance: Unifying role of ventricular septum. *J. Thorac. Cardiovasc. Surg.* **148**, 3166–3171.e4 (2014).
25. S. B. Brown, A. Raina, D. Katz, M. Szerlip, S. E. Wiegers, P. R. Forfia, Longitudinal shortening accounts for the majority of right ventricular contraction and improves after pulmonary vasodilator therapy in normal subjects and patients with pulmonary arterial hypertension. *Chest* **140**, 27–33 (2011).
26. L. Rosalia, C. Ozturk, J. Coll-Font, Y. Fan, Y. Nagata, M. Singh, D. Goswami, A. Mauskapf, S. Chen, R. A. Eder, E. M. Goffer, J. H. Kim, S. Yurista, B. P. Bonner, A. N. Foster, R. A. Levine, E. R. Edelman, M. Panagia, J. L. Guerrero, E. T. Roche, C. T. Nguyen, A soft robotic sleeve mimicking the haemodynamics and biomechanics of left ventricular pressure overload and aortic stenosis. *Nat. Biomed. Eng.* **6**, 1134–1147 (2022).
27. L. Rosalia, C. Ozturk, D. Goswami, J. Bonnemain, S. X. Wang, B. Bonner, J. C. Weaver, R. Puri, S. Kapadia, C. T. Nguyen, E. T. Roche, Soft robotic patient-specific hydrodynamic model of aortic stenosis and ventricular remodeling. *Sci. Robot.* **8**, eade2184 (2023).
28. P. T. Phan, M. T. Thai, T. T. Hoang, N. H. Lovell, T. N. Do, HFAM: Soft hydraulic filament artificial muscles for flexible robotic applications. *IEEE Access* **8**, 226637–226652 (2020).
29. J. Davies, M. T. Thai, H. Low, P. T. Phan, T. T. Hoang, N. H. Lovell, T. N. do, Bio-SHARPE: Bioinspired soft and high aspect ratio pumping element for robotic and medical applications. *Soft Robot.* **10**, 1055–1069 (2023).
30. K. T. Weber, Cardiac interstitium in health and disease: The fibrillar collagen network. *J. Am. Coll. Cardiol.* **13**, 1637–1652 (1989).
31. T. F. Robinson, S. M. Factor, E. H. Sonnenblick, The heart as a suction pump. *Sci. Am.* **254**, 84–91 (1986).
32. J. B. Pettigrew, The Croonian Lecture—On the arrangement of the muscular fibres of the ventricular portion of the heart of the mammal. *Proc. R. Soc. Lond.* **10**, 433–440 (1860).
33. G. D. Buckberg, H. C. Coghlan, F. Torrent-Guasp, The structure and function of the helical heart and its buttress wrapping. V. Anatomic and physiologic considerations in the healthy and failing heart. *Semin. Thorac. Cardiovasc. Surg.* **13**, 358–385 (2001).
34. F. Torrent-Guasp, G. D. Buckberg, C. Clemente, J. L. Cox, H. C. Coghlan, M. Gharib, The structure and function of the helical heart and its buttress wrapping. I. The normal macroscopic structure of the heart paper. *Semin. Thorac. Cardiovasc. Surg.* **13**, 342–357 (2001).
35. R. F. Rushmer, D. K. Crystal, C. Wagner, The functional anatomy of ventricular contraction. *Circ. Res.* **1**, 162–170 (1953).
36. D. Streeter, "The cardiovascular system: Gross morphology and fiber geometry of the heart" in *Handbook of Physiology, The Cardiovascular System I*, R. Berne, Ed. (American Physiological Society, 1979), pp. 61–112.
37. C. Mekkaoui, T. G. Reese, M. P. Jackowski, S. F. Cauley, K. Setsompop, H. Bhat, D. E. Sosnovik, Diffusion tractography of the entire left ventricle by using free-breathing accelerated simultaneous multisection imaging. *Radiology* **282**, 850–856 (2017).
38. J. D. Bayer, R. C. Blake, G. Plank, N. A. Trayanova, A novel rule-based algorithm for assigning myocardial fiber orientation to computational heart models. *Ann. Biomed. Eng.* **40**, 2243–2254 (2012).
39. H. Ashikaga, B. A. Coppola, B. Hopenfeld, E. S. Leifer, E. R. McVeigh, J. H. Omens, Transmural dispersion of myofiber mechanics: Implications for electrical heterogeneity in vivo. *J. Am. Coll. Cardiol.* **49**, 909–916 (2007).
40. M. Carlsson, M. Ugander, E. Heiberg, H. Arheden, The quantitative relationship between longitudinal and radial function in left, right, and total heart pumping in humans. *Am. J. Physiol. Heart Circ. Physiol.* **293**, H636–H644 (2007).
41. R. M. Lang, L. P. Badano, V. Mor-Avi, J. Afilalo, A. Armstrong, L. Ernande, F. A. Flachskampf, E. Foster, S. A. Goldstein, T. Kuznetsova, P. Lancellotti, D. Muraru, M. H. Picard, E. R. Rietzschel, L. Rudski, K. T. Spencer, W. Tsang, J. U. Voigt, Recommendations for cardiac chamber quantification by echocardiography in adults: An update from the American Society of Echocardiography and the European Association of Cardiovascular Imaging. *Eur. Heart J. Cardiovasc. Imaging* **16**, 233–271 (2015).
42. N. B. Ingels Jr., D. E. Hansen, G. T. Daughters II, E. B. Stinson, E. L. Alderman, D. C. Miller, Relation between longitudinal, circumferential, and oblique shortening and torsional deformation in the left ventricle of the transplanted human heart. *Circ. Res.* **64**, 915–927 (1989).
43. P. P. Sengupta, V. K. Krishnamoorthy, J. Korinek, J. Narula, M. A. Vannan, S. J. Lester, J. A. Tajik, J. B. Seward, B. K. Khandheria, M. Belohlavek, Left ventricular form and function revisited: Applied translational science to cardiovascular ultrasound imaging. *J. Am. Soc. Echocardiogr.* **20**, 539–551 (2007).
44. L. E. Hudsmith, S. E. Petersen, J. M. Francis, M. D. Robson, S. Neubauer, Normal human left and right ventricular and left atrial dimensions using steady state free precession magnetic resonance imaging. *J. Cardiovasc. Magn. Reson.* **7**, 775–782 (2005).
45. Y. Yu, S. Yu, X. Tang, H. Ren, S. Li, Q. Zou, F. Xiong, T. Zheng, L. Gong, Evaluation of left ventricular strain in patients with dilated cardiomyopathy. *J. Int. Med. Res.* **45**, 2092–2100 (2017).
46. M. D. Eggen, C. M. Swingen, P. A. Iaizzo, Analysis of fiber orientation in normal and failing human hearts using diffusion tensor MRI, in *2009 IEEE International Symposium on Biomedical Imaging: From Nano to Macro* (IEEE, 2009), pp. 642–645.
47. C. Von Deuster, E. Sammut, L. Asner, D. Nordsletten, P. Lamata, C. T. Stoeck, S. Kozerke, R. Razavi, Studying dynamic myofiber aggregate reorientation in dilated cardiomyopathy using in vivo magnetic resonance diffusion tensor imaging. *Circ. Cardiovasc. Imaging* **9**, e005018 (2016).
48. M. Hadjicharalambous, L. Asner, R. Chabiniok, E. Sammut, J. Wong, D. Peressutti, E. Kerfoot, A. King, J. Lee, R. Razavi, N. Smith, G. Carr-White, D. Nordsletten, Non-invasive model-based assessment of passive left-ventricular myocardial stiffness in healthy subjects and in patients with non-ischemic dilated cardiomyopathy. *Ann. Biomed. Eng.* **45**, 605–618 (2017).
49. K. M. Sveric, S. Ulbrich, M. Rady, T. Ruf, H. Kvakan, R. H. Strasser, S. Jellinghaus, Three-dimensional left ventricular torsion in patients with dilated cardiomyopathy—A marker of disease severity. *Circ. J.* **81**, 529–536 (2017).
50. P. Claus, A. M. S. Omar, G. Pedrizzetti, P. P. Sengupta, E. Nagel, Tissue tracking technology for assessing cardiac mechanics: Principles, normal values, and clinical applications. *JACC Cardiovasc. Imaging* **8**, 1444–1460 (2015).
51. M. Genet, L. C. Lee, R. Nguyen, H. Haraldsson, G. Acevedo-Bolton, Z. Zhang, L. Ge, K. Ordovas, S. Kozerke, J. M. Guccione, Distribution of normal human left ventricular myofiber stress at end diastole and end systole: A target for in silico design of heart failure treatments. *J. Appl. Physiol.* **117**, 142–152 (2014).
52. M. Carlsson, P. Cain, C. Holmqvist, F. Stahlberg, S. Lundback, H. Arheden, Total heart volume variation throughout the cardiac cycle in humans. *Am. J. Physiol. Heart Circ. Physiol.* **287**, H243–H250 (2004).
53. T. J. Buchner, S. Rogler, S. Weirich, Y. Armati, B. G. Cangan, J. Ramos, S. T. Twiddy, D. M. Marini, A. Weber, D. Chen, G. Ellson, J. Jacob, W. Zengerle, D. Katalichenko, C. Keny, W. Matusik, R. K. Katzschmann, Vision-controlled jetting for composite systems and robots. *Nature* **623**, 522–530 (2023).
54. X. Liu, Z. Li, Assessment of cardiac twist in dilated cardiomyopathy using velocity vector imaging. *Echocardiography* **27**, 400–405 (2010).
55. S. Sawatani, G. Mandell, E. Kusaba, W. Schraut, P. Cascade, W. J. Wajszczuk, A. Kantrowitz, Ventricular performance following ablation and prosthetic replacement of right ventricular myocardium. *Trans. Am. Soc. Artif. Intern Organs* **20**, 629–636 (1974).
56. F. Torrent-Guasp, M. J. Kocica, A. Corno, M. Komeda, J. Cox, A. Flotats, M. Ballester-Rodes, F. Carreras-Costa, Systolic ventricular filling. *Eur. J. Cardiothorac. Surg.* **25**, 376–386 (2004).
57. P. Boettler, P. Claus, L. Herbots, M. M. Laughlin, J. D'hooge, B. Bijnens, S. Y. Ho, D. Kececioglu, G. R. Sutherland, New aspects of the ventricular septum and its function: An echocardiographic study. *Heart* **91**, 1343–1348 (2005).
58. I. G. McDonald, The shape and movements of the human left ventricle during systole: A study by cineangiography and by cineradiography of epicardial markers. *Am. J. Cardiol.* **26**, 221–230 (1970).
59. P. P. Sengupta, A. J. Tajik, K. Chandrasekaran, B. K. Khandheria, Twist mechanics of the left ventricle: Principles and application. *JACC Cardiovasc. Imaging* **1**, 366–376 (2008).
60. G. Buckberg, J. I. Hoffman, A. Mahajan, S. Saleh, C. Coghlan, Cardiac mechanics revisited: The relationship of cardiac architecture to ventricular function. *Circulation* **118**, 2571–2587 (2008).
61. Y. Notomi, M. G. Martin-Miklovic, S. J. Oryszak, T. Shiota, D. Deserranno, Z. B. Popovic, M. J. Garcia, N. L. Greenberg, J. D. Thomas, Enhanced ventricular untwisting during exercise: A mechanistic manifestation of elastic recoil described by Doppler tissue imaging. *Circulation* **113**, 2524–2533 (2006).
62. S.-J. Dong, P. S. Hees, C. O. Siu, J. L. Weiss, E. P. Shapiro, MRI assessment of LV relaxation by untwisting rate: A new isovolumic phase measure of τ. *Am. J. Physiol. Heart Circ. Physiol.* **281**, H2002–H2009 (2001).

63. Y. Notomi, Z. B. Popović, H. Yamada, D. W. Wallick, M. G. Martin, S. J. Oryszak, T. Shiota, N. L. Greenberg, J. D. Thomas, Ventricular untwisting: A temporal link between left ventricular relaxation and suction. *Am. J. Physiol. Heart Circ. Physiol.* **294**, H505–H513 (2008).
64. G. D. Buckberg, J. I. Hoffman, H. C. Coghlan, N. C. Nanda, Ventricular structure–function relations in health and disease: Part I. The normal heart. *Eur. J. Cardiothorac. Surg.* **47**, 587–601 (2015).
65. E. R. Chamberlain, US Patent 20020061503A1 (2004).
66. K. Narayanan, K. Reinier, C. Teodorescu, A. Uy-Evanado, R. Aleong, H. Chugh, G. A. Nichols, K. Gunson, B. London, J. Jui, S. S. Chugh, Left ventricular diameter and risk stratification for sudden cardiac death. *J. Am. Heart Assoc.* **3**, e001193 (2014).
67. A. Mesa, C. Jessurun, A. Hernandez, K. Adam, D. Brown, W. K. Vaughn, S. Wilansky, Left ventricular diastolic function in normal human pregnancy. *Circulation* **99**, 511–517 (1999).
68. M. Pascual, D. A. Pascual, F. Soria, T. Vicente, A. M. Hernández, F. J. Tébar, M. Valdés, Effects of isolated obesity on systolic and diastolic left ventricular function. *Heart* **89**, 1152–1156 (2003).
69. W. P. Hood Jr., C. E. Rackley, E. L. Rolett, Wall stress in the normal and hypertrophied human left ventricle. *Am. J. Cardiol.* **22**, 550–558 (1968).

Acknowledgments: We acknowledge the support of A. Al-Abed and S. Dokos for computational simulation. M.T.T., T.T.H., and C.C.N. would like to thank the Science and Technology Scholarship Program for Overseas Study for Master's and PhD degrees, VinUniversity, Vingroup, Vietnam. **Funding:** This work was supported by the UNSW Scientia Fellowship Grant (PS46197-A), Vanguard Grant from the National Heart Foundation of Australia (RG204224), and UNSW 3Rs Grant (RG192608-L). **Author contributions:** Conceptualization: J.J.D., M.T.T., T.T.H., C.C.N., P.T.P., K.Z., B.S., A.J., E.N., and T.N.D. Methodology: J.J.D., M.T.T., T.T.H., C.C.N., and B.S. Investigation: J.J.D., M.T.T., T.T.H., C.C.N., B.S., and T.N.A.M.V. Visualization: J.J.D., B.S., M.T.T., T.T.H., and C.C.N. Funding acquisition: T.N.D. Project administration: T.N.D. and J.J.D. Supervision: T.N.D. and N.H.L. Writing—original draft: J.J.D. Writing—review and editing: J.J.D., M.T.T., T.T.H., C.C.N., P.T.P., Y.-C.T., M.S., C.H., H.-P.P., N.H.L., and T.N.D. **Competing interests:** The authors declare that they have no competing interests. **Data and materials availability:** All data and information necessary to reproduce this study are available in the main text or the Supplementary Materials.

Submitted 2 February 2024
Accepted 30 August 2024
Published 25 September 2024
10.1126/scirobotics.ado4553

Science Robotics

Soft robotic artificial left ventricle simulator capable of reproducing myocardial biomechanics

James Davies, Mai Thanh Thai, Bibhu Sharma, Trung Thien Hoang, Chi Cong Nguyen, Phuoc Thien Phan, Thao Nhu Anne Marie Vuong, Adrienne Ji, Kefan Zhu, Emanuele Nicotra, Yi-Chin Toh, Michael Stevens, Christopher Hayward, Hoang-Phuong Phan, Nigel Hamilton Lovell, and Thanh Nho Do

Sci. Robot. **9** (94), eado4553. DOI: 10.1126/scirobotics.ado4553

Editor's summary

Cardiac devices and interventions are often dependent on the use of animal models and ex vivo tissue for testing and development. Moreover, surgical training for procedure-specific skills also relies on animal tissue. Davies *et al.* have developed a soft robotic device that can mimic the left ventricle of the heart and reproduce cardiac motion as well as physiological hemodynamic conditions. They demonstrated the ability to simulate conditions of healthy and diseased heart states, with the potential to counter the need for animal models to develop cardiac devices. —Amos Matsiko